Phase coexistence induced surface roughness in V_2O_3/Ni magnetic heterostructures

K. Ignatova,[1] E. Vlasov,[2] S. D. Seddon,[3] N. Gauquelin,[2] J. Verbeeck,[2]
D. Wermeille,[4,5] S. Bals,[2] T. P. A. Hase,[6] and U. B. Arnalds[1]

[1]*Science Institute, University of Iceland, Dunhaga 3, 107 Reykjavik, Iceland*
[2]*EMAT and NANOlab Center of Excellence, University of Antwerp, Groenenborgerlaan 171, Antwerp, Belgium*
[3]*TU Dresden, Institute of Applied Physics, Nöthnitzer Strasse 61, 01187 Dresden, Germany*
[4]*XMaS, The UK Materials Science Facility, European Synchrotron Radiation Facility, F-38043 Grenoble, France*
[5]*Dept of Physics, University of Liverpool, Oliver Lodge, Liverpool L69 7ZE, United Kingdom*
[6]*Department of Physics, University of Warwick, Coventry CV4 7AL, United Kingdom*

We present an investigation on the microstructure changes in V_2O_3 as it goes through its inherent structural phase transition. Using V_2O_3 films with well-defined crystal structure deposited by reactive magnetron sputtering on *r*-plane Al_2O_3 substrates, we study the phase coexistence region and its impact on the surface roughness of the films and the magnetic properties of overlying Ni magnetic layers in V_2O_3/Ni hybrid magnetic heterostructures. The simultaneous presence of two phases in V_2O_3 during its structural phase transition was identified with high resolution x-ray diffraction and led to an increase in surface roughness observed using x-ray reflectivity. The roughness is maximum at the midpoint of the transition. In V_2O_3/Ni hybrid heterostructures, we find a concomitant increase in the coercivity of the magnetic layer correlated with the increased roughness of the V_2O_3 surface. The chemical homogeneity of the V_2O_3 is confirmed through transmission electron microscopy analysis. High-angle annular dark field imaging and electron energy loss spectroscopy reveal an atomically flat interface between Al_2O_3 and V_2O_3, as well as a sharp interface between V_2O_3 and Ni.

I. INTRODUCTION

Transition metal oxides in the vanadium oxide family comprise an interesting class of materials that exhibit multiple oxidation states[1]. These materials are primarily recognized for their triple transition: a first-order metal-insulator transition (MIT), a structural phase transition (SPT), and a magnetic transition. These transitions typically occur simultaneously but can be modified or suppressed, through techniques such as doping and applying stress[2–6]. In both bulk and thin film forms, vanadium oxides have found applications in memristors, battery electrodes, supercapacitors[7] and other memory-related technologies. The incorporation of vanadium oxide composite thin films with a magnetic layer presents numerous additional possibilities for utilizing nano-devices in sensor technology, antiferromagnetic spintronics[8,9], medical applications[10], Mott-based memory devices[11], and neuromorphic computing[12–14].

Extensive research has been conducted to understand the underlying mechanisms of the MIT and the SPT in vanadium oxide as well as to investigate the impact of phase transitions in vanadium oxides on the magnetic characteristics of hybrid magnetic heterostructures[15]. The underlying phase transitions are emerging as an increasingly potent mechanism for manipulating essential characteristics of epitaxial heterostructures containing vanadium oxide[16–20]. Experimental evidence has demonstrated that structural phase transitions and surface-induced roughness can directly influence magnetic overlayers, leading to alterations in their internal anisotropy, coercivity as well as an emerging exchange bias[16,19–23]. Gaining a comprehensive understanding of the intricate detailed microstructure-property relationships is crucial for fully exploiting the effects of phase transitions in vanadium oxides on systems integrated with these phase-change materials.

For our study, we focus on thin film vanadium sesquioxide (V_2O_3) with well-defined crystal structure, which undergoes a structural transition from a low-temperature insulating/antiferromagnetic phase to a high-temperature metallic/paramagnetic phase. During this transition, the crystalline structure of V_2O_3 undergoes a transformation from a single monoclinic (MC) phase to a coexistence of rhombohedral and monoclinic phases at approximately 130 K which eventually transitions into a single rhombohedral (RH) phase structure[21]. Here we investigate the interplay between the microstructure of the V_2O_3 films and their structural properties during the phase transition. Specifically, we examine the changes in the microstructure during the phase coexistence region of the V_2O_3 layer and how these changes correlate with alterations in the magnetic properties of overlying magnetic layers in V_2O_3/Ni heterostructures.

II. MATERIALS AND METHODS

The V_2O_3 and V_2O_3/Ni films were grown on *r*-plane Al_2O_3 $[1\bar{1}02]$ substrates using reactive direct current (dc) magnetron sputtering for the V_2O_3 layer and conventional dc magnetron sputtering for the Ni layer. Additionally, a Zr capping layer was deposited to prevent oxidation of the Ni layer. The substrates were annealed in air at 1200 °C for 24 hours. The growth process was carried out in a custom-built chamber[24], utilizing a high-purity 3-inch vanadium (99.99%) and a high-purity 3-inch nickel (99.99%) sputtering targets. Prior to de-

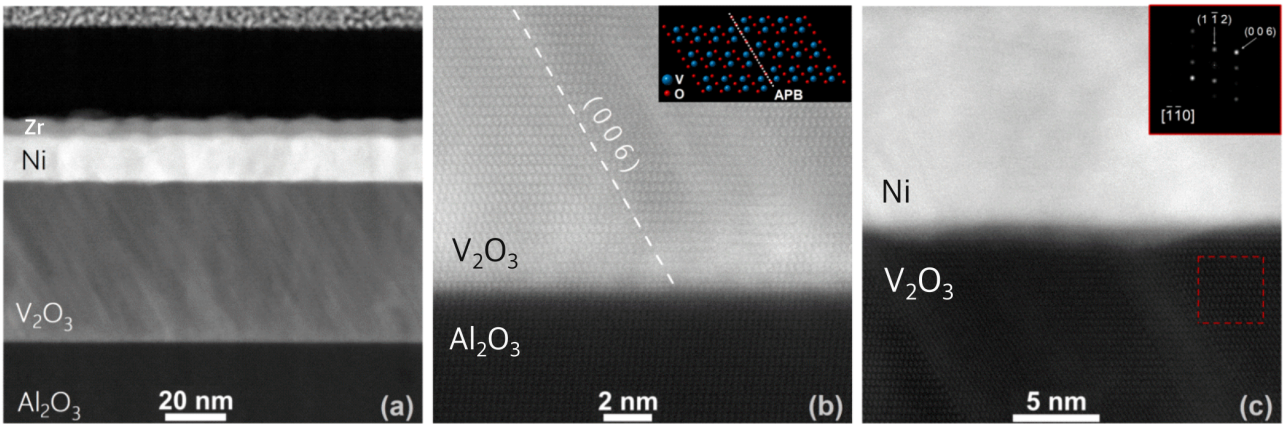

FIG. 1. HAADF-STEM images of (a) the cross-section of the V_2O_3/Ni/Zr thin film on the Al_2O_3 r-plane substrate and (b) the Al_2O_3/V_2O_3 and (c) the V_2O_3/Ni interfaces. The HAADF-STEM signal intensity is proportional to atomic number and portrayed in the greyscale of the images. The dashed line in (b) illustrates the placement of an anti-phase boundary in the V_2O_3, with the possible atom arrangement schematics illustrated in the inset. The inset in (c) shows a diffractogram obtained by Fourier transforming the image from the red square region in the V_2O_3 layer indexed as rhombohedral V_2O_3.

position, the base pressure of the chamber was below 4×10^{-6} Pa. The substrates underwent pre-baking under vacuum in the sputtering chamber at a temperature of 610 °C for $\sim$ 60 minutes prior to any growth. The V_2O_3 was deposited at a temperature of 610 °C, whilst the Ni and Zr layers were deposited at room temperature after allowing the sample to cool down under ultra-high vacuum. An identical reference sample consisting solely of the V_2O_3 layer was deposited following the same recipe. X-ray reflectivity (XRR) analysis showed the heterostructure film stack to be composed of a 49 nm thick V_2O_3 layer, followed by a 13 nm Ni layer, and finally a 6 nm thick Zr capping layer.

The structural properties of the V_2O_3 and V_2O_3/Ni films were examined as a function of temperature using high-resolution double-axis X-ray diffraction (XRD) and reflectivity (XRR) measurements at the BM28 (XMaS) beamline at the European Synchrotron Radiation Facility (ESRF) in Grenoble, France[25]. The photon energy was chosen to be 12.4 keV, corresponding to a wavelength of 1 Å. The XRR profiles were fitted using the GenX software[26]. High-resolution 3-dimensional reciprocal space mapping (3D-RSM) was employed to investigate the crystal microstructure and its structural evolution across the temperature-driven phase transition in the V_2O_3 and V_2O_3/Ni films. The surface morphology of the specimens was examined using atomic force microscopy (AFM) in contact mode at room temperature.

The stoichiometric composition and crystalline quality at the sub-nm lateral scale of the films were investigated by scanning transmission electron microscopy (STEM), using high-angle annular dark-field (HAADF-STEM) imaging, energy dispersive x-ray analysis (STEM-EDX) and electron energy loss spectroscopy (EELS). The HAADF-STEM imaging, EELS, and STEM-EDX measurements were conducted on a double aberration-corrected Thermo Fischer Scientific X-Ant-EM instrument operated at 120 kV and equipped with a GIF Enfinium EELS spectrometer. The TEM lamellas were prepared by focused ion beam (FIB) milling. The magnetic properties of the V_2O_3/Ni bilayer were characterized using the longitudinal magneto-optical Kerr effect (MOKE) as a function of azimuth angle at room temperature. Furthermore, the temperature-dependent magnetic characterization was performed using vibrating sample magnetometry (VSM) and a custom-built system for measuring the longitudinal MOKE signal at low temperatures.

III. EXPERIMENTAL RESULTS

A. Phase and microstructure investigation

Figure 1(a) shows an overview cross-sectional HAADF-STEM image of the V_2O_3/Ni/Zr heterostructure on the Al_2O_3 substrate. Figure 1(b) and Figure 1(c) show higher magnification images at the Al_2O_3/V_2O_3 and V_2O_3/Ni interfaces, respectively. The data clearly reveal both the crystalline nature of the film and the high quality of the interfaces. The TEM images were taken in the $[\bar{1}\bar{1}0]$ zone axis of the Al_2O_3 sapphire substrate.

The chemical and oxidation states of the V_2O_3 and Ni layers were investigated using EELS. EELS spectra were recorded at different locations of the V_2O_3, in the middle of the layer and near both interfaces, as shown in Fig. 2. The observed V-L_3 energy loss edge is 517.48 eV and O-K edges consist mainly of two peaks, which correspond well with the fingerprint feature of rhombohedral corundum V_2O_3[27–29]. At the nanoscale, the EELS analysis indicates that the oxidation state of vanadium does not vary across the entire film (see Fig. 2), revealing no evidence of other non-stoichiometric parasitic phases of vanadium oxide in the film. We can therefore conclude that the

V_2O_3 layer is chemically homogeneous in our samples. EELS structure evolution spectra recorded for the Ni and other interfaces in the film are shown in Figure S1 and Figure S2 of the Supplementary Material. After extended exposure, the top capping layer undergoes oxidation, as confirmed by the EELS analysis. Consequently, all scans were analyzed using a model that incorporates ZrO_2 atop the heterostructure. Notably, there is no presence of a NiO layer across the film (see Supplementary Material Figure S1). The analysis of the HAADF images together with line profiles retrieved from EELS reveal the quality of the interfaces. It is evident that the Al_2O_3/V_2O_3 interface is atomically flat and the V_2O_3/Ni interface has a well-defined boundary between the layers with negligible intermixing. The extent of inter-diffusion between the V_2O_3 and Ni layers does not exceed 1.5 nm (see Supplementary Material Figure S1 and S2). The thicknesses of the V_2O_3/Ni film obtained from the STEM measurements are in agreement with thickness determined from XRR data performed at room temperature of 49 nm and 13 nm, respectively.

The STEM images show striped patterns with staircase-like features in the V_2O_3 layer (Fig. 1(b)). This structural feature is a typical signature of the presence of symmetry-breaking anti-phase boundaries (APB) that emerge at the Al_2O_3/V_2O_3 interface, with the displacement vector parallel to the $< 001 >$ direction[30,31]. Neighboring domains separated by the APB are displaced by half of a unit cell along the (006) plane, as demonstrated schematically in the inset in Fig. 1(b). Other microstructure symmetry-breaking effects, such as crystallographic twinning, have been found previously in VO_2 films grown on c-plane Al_2O_3 substrates[32]. In our case a similar parallel columnar-like microstructure of the V_2O_3 layer is

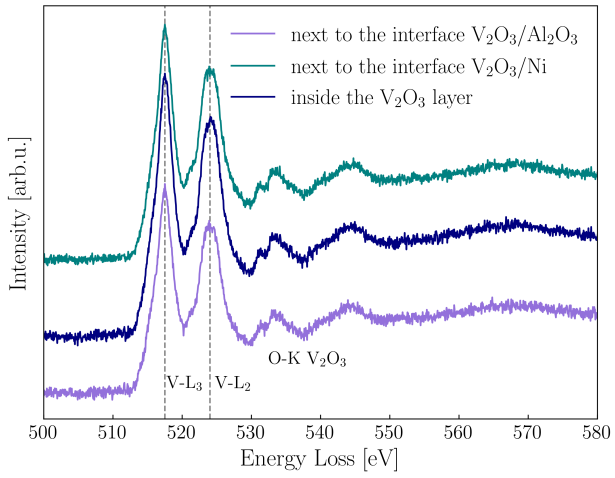

FIG. 2. STEM-EELS spectra with indicated V-L and O-K edges taken from the V_2O_3/Ni interface and the V_2O_3 interior. The spectra are corrected for background and taken at room temperature for the V_2O_3/Ni film grown on the r-plane of the Al_2O_3 substrate.

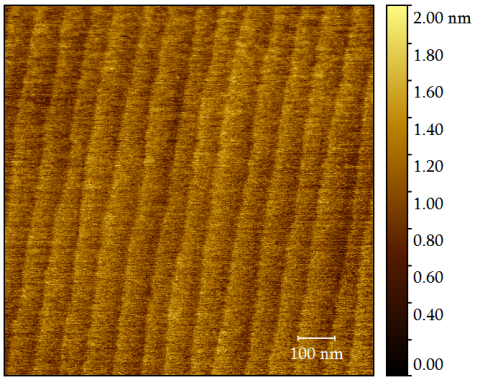

FIG. 3. $5 \times 5\ \mu m^2$ atomic force microscopy image of r-plane sapphire Al_2O_3 substrate annealed for 24 hours at 1200°C. The annealed surface exhibits atomically flat terraces, with each terrace ∼100 nm in width.

observed for the V_2O_3 films grown on c-plane sapphire substrates (see Supplementary Material Figure S3) with no presence of twinning or APB defects. Further details on the structural and magnetic properties of c-plane V_2O_3/Ni heterostructure can be found elsewhere[20]. Figure 1(b) reveals no twinning in the V_2O_3 layer grown on Al_2O_3 r-plane, only showing anti-phase boundaries at an angle of 59.04° with the surface plane corresponding well to the angle between the film surface normal (012) and (006) plane of 58.59°. APBs in V_2O_3 films grown on Al_2O_3 c-plane substrates have been previously observed, with APBs being identified in the planar view of the c-plane[33]. Multiple mechanisms can induce the formation and nucleation process of APBs. Typically, the formation of APBs appears during thin film growth[34,35]. For V_2O_3 films deposited onto annealed Al_2O_3 substrates the most likely reason for the formation of APBs in the V_2O_3 layer is related with the Al_2O_3 r-plane substrate due to its multi-step, terrace-like surface structure formed by the annealing at 1200°C, as can be seen from Figure 3.

B. Structural evolution

The crystal structural evolution of the film through the phase transition was investigated by performing X-ray diffraction measurements as a function of temperature from 30 K to 277 K. Figure 4 shows a sub-set of the XRD scans recorded along the surface normal from 70 K to 180 K. The data show clear single phase behavior at low and high temperatures arising from the low temperature monoclinic and high temperature rhombohedral phases. Additional powder-like peaks originating from the Be vacuum capsule are evident across the entire temperature range (see Fig. 4). It is crucial to note that the Ni layer exhibits a textured (111) orientation, as evidenced by a weak peak observed around 44.5°, which can be attributed to the Ni (111) reflection (see Supplementary Material Figure S4).

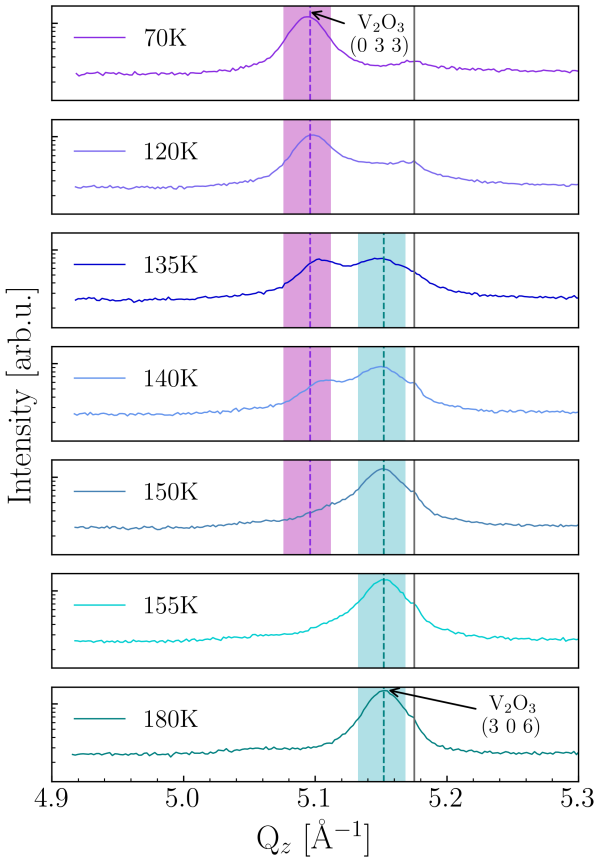

FIG. 4. Temperature-dependent x-ray diffraction scans recorded for the V_2O_3/Ni film as a function of temperature across the SPT of V_2O_3. Pink and cyan bars indicate the diffraction peaks for the monoclinic and rhombohedral phases of the V_2O_3 at low and high temperatures, respectively. Broken lines indicate the XRD peak positions derived by the fitting with a Pearson type VII function of the monoclinic V_2O_3 (0 3 3) at low temperatures and the rhombohedral V_2O_3 (3 0 6) at high temperatures. Straight grey lines indicate Be powder peak positions arising from scattering from the beryllium vacuum capsule.

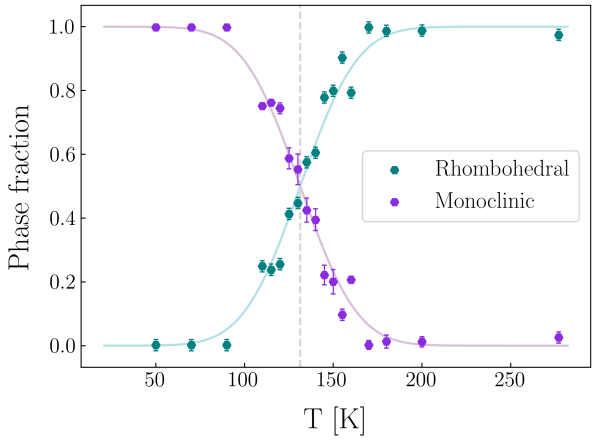

FIG. 5. Relative intensities of V_2O_3 (0 3 3) and V_2O_3 (3 0 6) Bragg peaks observed upon heating in the V_2O_3/Ni film. The dashed line indicates the temperature where the ratio of monoclinic and rhombohedral V_2O_3 phases are equal and it is at ~ 130 K. The dependency of the phase fractions with temperature was modeled using a cumulative skewed normal distribution function. The function is symmetric within uncertainty, with a transition width of 12.7 K, centered at 131.4 K.

The transition from the low temperature phase begins at about 110 K and extends up to about 155 K at which point the layer has fully transformed to the rhombohedral phase (see Fig. 4). The peak intensities and locations of the two phases (indicated by dashed lines in the graphs) were extracted by fitting the XRD data to the sum of two Pearson VII peaks. Figure 5 shows the crystallographic phase fractions determined from fits to the peaks shown in Figure 4 and normalized by their sum. The dependence of the phase fractions with temperature was modeled using a cumulative skewed normal distribution function to account for any asymmetry, with α as a parameter that determines the degree and direction of skewness. Further details regarding the definition of skewed normal distribution can be found in the Supplementary Material (Eq. (1)). Both data were fitted simultaneously with the phase fraction of the rhombohedral phase assumed to follow the complementary function of the monoclinic phase fraction. Although the fit function has no physical meaning it captures the overall features of the structural transition well. The function was found to be symmetric within uncertainty with the shape parameter, $\alpha = -0.1 \pm 0.6$. The standard deviation, or width, of the transition is 12.7 ± 0.3 K and the centre of the transition determined using the centre of mass of the fit function is 131.4 ± 0.5 K. The corresponding temperature for the non-capped V_2O_3 layer is ~ 133 K (see supplementary figure S5). XRR intensity profiles for the single V_2O_3 layer film and the V_2O_3/Ni film were acquired at different temperatures upon heating from 30 K to 200 K. The thickness and roughness values were derived by fitting the XRR data using the GenX software package[26], with an example shown in Figure 6 (a). The thickness and roughness of the V_2O_3 layer in the V_2O_3/Ni film as a function of temperature are shown in Figure 6(b) and (c). A slight decrease in layer thickness by 1.5% upon heating is observed for both specimens which is consistent with changes in the lattice parameter of the monoclinic and rhombohedral phases[36,37]. The same function that was used to model the phase fractions determined from XRD in Fig. 5 is redrawn in Fig. 6(b), simply scaled in amplitude. The close agreement of the line with the data shows that there is a clear correlation between the phase fraction and the thickness of the V_2O_3 layer. Simultaneously, across the phase coexistence region, an elevation in the roughness of the V_2O_3 layer determined from the XRR fitting was also observed, which was maximized at the midpoint of the transition. The correlation between the phase fractions and the roughness enhancement at the

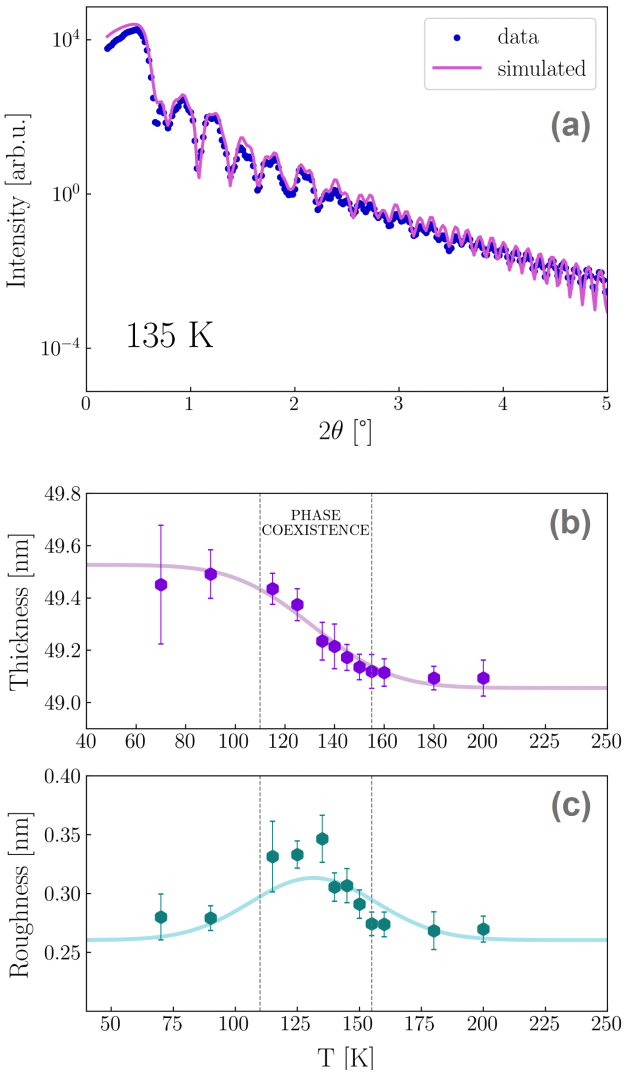

FIG. 6. (a) XRR data recorded for the V_2O_3/Ni structure at 135 K and fit using GenX[26]. The corresponding x-ray scattering length density profile of the film at 135 K is shown in Supplementary Material Figure S6. (b) and (c) show the thickness and the roughness values of the V_2O_3 layer derived from the fit of the XRR profiles as a function of temperature, respectively. The error bars represent estimated systematic errors calculated in the fitting. Dashed lines indicate where the fractions of either of the two coexisting phases correspond to 5 %.

middle of the transition is further demonstrated in the solid line shown in Fig. 6(c) which is the scaled derivative of the fit function used to model the phase fractions in Fig. 5 and the layer thickness in Fig. 6(b).

C. Reciprocal space mapping

In order to observe the coexistence of the both phases and investigate further any lateral changes in the crystal or film structure, 3D-reciprocal space volumes of the scattering around the symmetric and asymmetric V_2O_3 Bragg reflections were recorded as a function of temperature. Reciprocal space volumes were also recorded for single layer films (see Supplementary Material Figure S7). Several scans were combined and data binned into cubic voxels of reciprocal space defined in the laboratory frame with the Q_z aligned with the surface normal and with Q_x and Q_y orthogonal directions in the plane of the sample with Q_x coincident with the incident beam. With respect to the rhombohedral crystal planes, Q_z is parallel to the 306 direction and Q_x aligned to the $\bar{1}20$ direction.

Figure 7 shows representative reciprocal space maps (RSMs) reduced into 2D by integrating the third reciprocal space direction for the V_2O_3/Ni film. The RSMs are shown for temperatures below the transition, at the transition midpoint, and above the transition. The data is generally clearer in the RSMs recorded in the vicinity of the symmetric peaks which are displayed in the left-hand panel of Figure 7. The sapphire substrate is the sharp peak at $Q_z = 5.41$ Å^{-1} and $Q_x = Q_y = 0$ Å^{-1}. The film peaks are seen as weaker reflections at lower Q_z. The splitting, corresponding to the transition between the low and high temperature phases seen in the 1-D projections shown in Fig. 4 is again clear. The weak streak at $Q_z = 5.17$ Å^{-1} is the powder line from the Be vacuum dome. However, the projections for the asymmetric peak masks the clear splitting due to the projection of the scattering vector into these directions but a distinct broadening is observed during the transition accompanied by a shift in the peak position from the low-temperature to the high-temperature phase.

In addition to the out-of-plane Q_z information, the RSMs provide further information on the lateral properties of the film through projections into Q_x and Q_y. Such in-plane data includes details on the mosaic, any lateral crystallographic periodicities or correlations, but also film strain. Thus, any domain formation in the V_2O_3 that could arise during the transition can therefore be observed in changes to the RSM film peak in the Q_x and Q_y directions as the material progresses between the two different phases. Specifically, any lateral periodic domain formation (as e.g. discussed in ref.[38]) would result in secondary peaks observed in the Q_x and Q_y scans while incoherent domain formation[39] would result in changes in the peak widths or form. The scans show no secondary peaks or changes in the lateral spread of the RSM peaks, therefore eliminating any short length scale periodicity or domain formation during the nano-scale phase formation and that the mosaic dominates the peak structure at all temperatures and remains unchanged during the phase transition.

D. Magnetic properties across the SPT

Any change to the surface morphology of the V_2O_3 layer will impact any crystalline overlayer by introducing

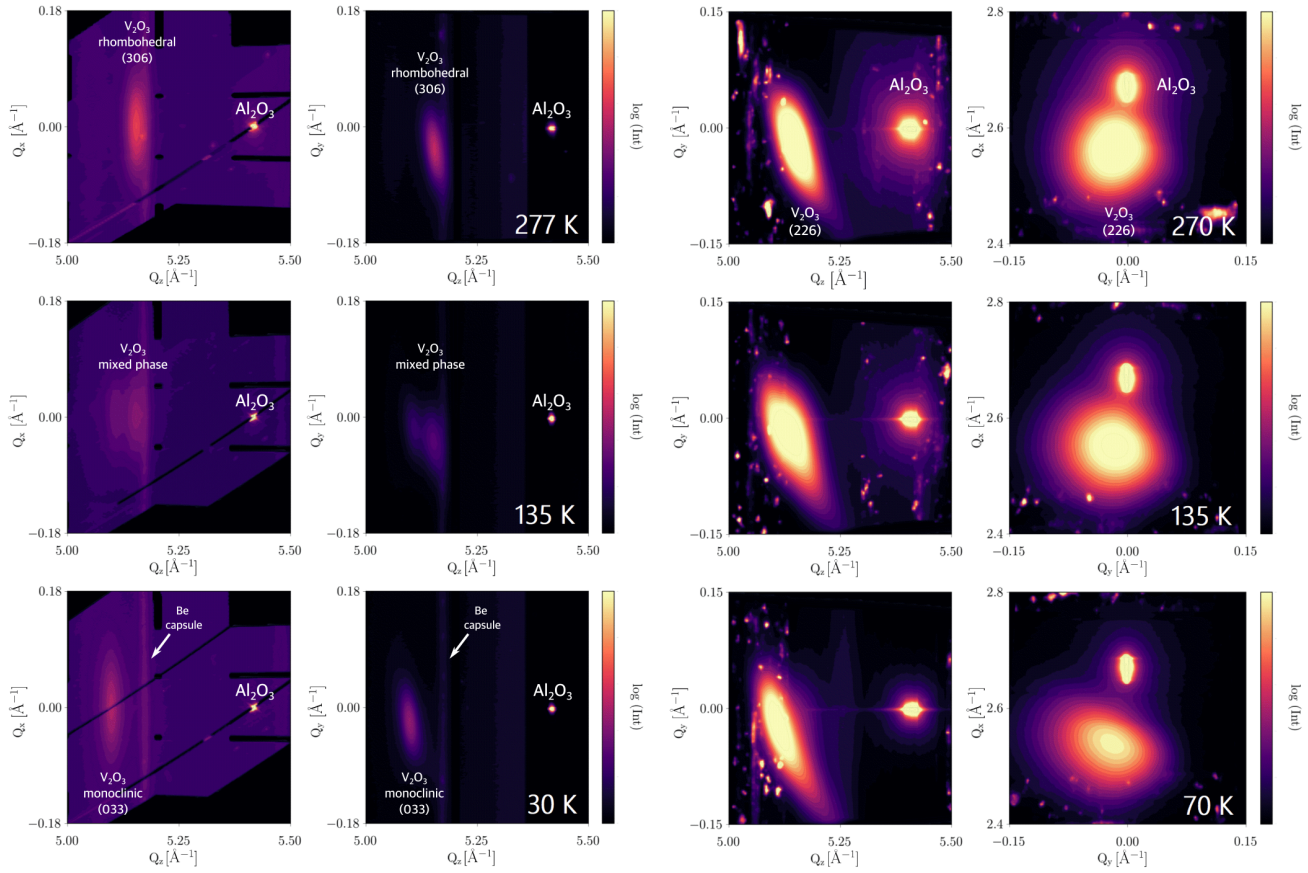

FIG. 7. 2D projections of 3D reciprocal space maps of the V_2O_3/Ni film recorded at different temperatures upon heating across the phase transition. Peaks are indexed to the rhombohedral structure for convenience. Left: RSM scans recorded for the symmetric (3 0 6) peak of V_2O_3 together with the Al_2O_3 substrate peak. Right: RSM scans recorded for the asymmetric (2 2 6) peak of V_2O_3. The scans for the symmetric (3 0 6) peak reveal a clear splitting for the two phases as in the XRD scans shown in Fig. 4.

interface strain. In the case of a magnetic material such as Ni, roughness contributes a significant factor with the enhanced roughness arising from the height difference of different domains during the transition inducing pinning centers, thereby enhancing the coercivity of the magnetic material. Figure 8 shows the coercivity of the magnetic layer derived from hysteresis loops recorded as a function of temperature. A representative magnetic hysteresis curve measured at 130 K is presented in the supplementary material (see Figure S8). The coercivity exhibits the expected decrease with increasing temperature as is generally observed for Ni films as more thermal energy becomes available. In addition to the expected temperature dependent decrease, a notable perturbation in the coercivity is observed across the mixed phase region with a peak occurring at a temperature coinciding with the structural phase transition in the V_2O_3. This temperature range of enhanced coercivity corresponds well to the phase coexistence region observed from XRD and the increased roughness seen in the XRR data as highlighted by the shaded region which corresponds to the 90% confidence interval determined from the phase fraction function shown in Figure 4.

IV. DISCUSSION

The temperature of the SPT is defined as that where the rhombohedral and the monoclinic phases are evenly contributed. As illustrated in Figure 4, the center of the transition is at a temperature of approximately 130 K. Similar analysis of data for the V_2O_3 single layer film (see Supplementary Material Figure S5) yields a transition temperature of 133 K. These results are consistent with the expected phase transformation of V_2O_3 as observed in structural characterization, resistivity and magnetic changes[20,21,40].

Within the region where both phases coexist, an increase in the roughness of the V_2O_3 layer is observed (Fig. 6(c)) with a maximum located at the transition midpoint. The increased roughness is attributed to the coexistence of the two phases in different regions of the

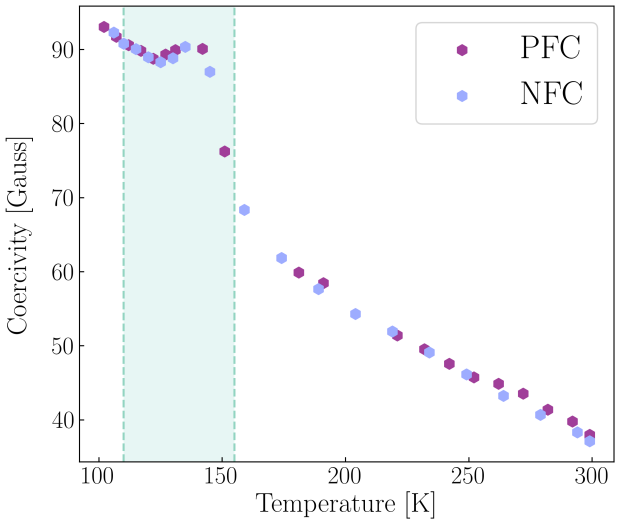

FIG. 8. Coercivity of the V_2O_3/Ni film extracted from magnetization loops recorded using low-temperature MOKE measurements as a function of increasing temperature after positive field cooling (PFC) under an applied field of 400 G and negative field cooling (NFC) with a field of −400 G along the easy axis. In addition to the general trend of reduced coercivity with increasing temperature from $H_c = 92$ G at 80 K down to $H_c = 35$ G at room temperature the presence of the clear peak in coercivity in temperature range of the SPT of the V_2O_3 layer is observed. This coercivity maximum across the SPT was verified by carrying out both MOKE and VSM measurements. Cyan dashed lines indicate the 90% confidence interval determined from the phase fraction function shown in Fig. 4.

film. A further analysis of the XRD data shows no apparent differences in the peak widths in Q_z for both phases (Fig. 4) across the entire temperature range. This indicates that when part of the film transitions, it does so across the entire film thickness. There is also little change in the in-plane scattering as seen in the RSMs suggesting that the lateral size of the transitioning regions are greater than the coherence length of the x-rays which is some tens of microns. The V_2O_3 surface in the mixed-phase regime is therefore composed of pillars of expanded rhombohedral phase and the original monoclinic phase. This results in an uneven interface profile which evolves with temperature and is most disordered when the ratio of the two phases is equal, i.e. at the mid point of the transition corresponding to the SPT.

The coercivity, shown in Fig. 8, exhibits a clear peak at a temperature corresponding to the structural phase transition in the V_2O_3 with a maxima at 135 K driven by the morphology of the V_2O_3/Ni interface. The peak in coercivity extends to approximately 155 K and at higher temperatures follows a general trend of reduced coercivity with increasing temperature. In addition to the peak in coercivity the data show a strain related shift in coercivity below and above the transition as has been observed in similar systems[20,22].

Confirmation of the importance of the roughness is found by comparing this study of the coercivity with our previous work on V_2O_3/Ni films grown on sapphire Al_2O_3 substrates with c-plane [0001] surface orientation under the same conditions as those reported here on sapphire r-plane [1$\bar{1}$02] substrates with nearly the same V_2O_3 thickness of ∼58 nm[20]. Whilst the V_2O_3 undergoes the same mixed phase transition for the two cases, when grown on c-plane [0001] the expansion of the V_2O_3 film along the surface normal is significantly reduced due to the epitaxy. Thus the morphology of the interface is smoother and more uniform with much less disorder introduced into the epitaxial Ni overlayer resulting in V_2O_3/Ni heterostructures grown on c-plane having more isotropic magnetic properties. In contrast, and as described here the r-plane V_2O_3/Ni films display a stronger tendency for nanoscale phase formation due to the increased interface roughness of the V_2O_3 layer during the transition. HAADF-STEM imaging also showed clear signs of anti-phase boundaries within the V_2O_3 layer on r-plane substrates while such boundaries were not observed for identical c-plane film structures. These boundaries can act as phase coexistence boundaries for adjacent regions undergoing transitions at different temperatures, thereby contributing to the observed increase in surface roughness during the transition.

V. CONCLUSIONS

In conclusion, we have investigated the microstructure and structural phase coexistence of the V_2O_3 layer in the V_2O_3/Ni system grown on r-plane sapphire, as well as the magnetic properties of the magnetic Ni layer in relation to the microstructure and structural behavior of the V_2O_3 during the SPT. As the V_2O_3 transitions from the low-temperature phase to the high-temperature phase the film thickness determined from XRR measurements decreases in accordance with the phase fractions determined from XRD measurements. Within the phase coexistence region, an increase in the roughness of the V_2O_3 layer is observed, reaching its maximum at the middle of the transition. This increased roughness is attributed to the different thicknesses of the two concurrent phases in V_2O_3 during the transition. The observed enhanced roughness follows the derivative of the skewed normal distribution function used to fit the phase fraction data illustrating that the roughness takes a maximum value at the middle of the transition.

In the temperature range of 110 K to 155 K, corresponding to the phase coexistence of V_2O_3, a notable peak of enhanced coercivity is observed. This peak is attributed to the transition occurring in the phase coexistence region, which is accompanied by increased roughness in the V_2O_3 layer, causing significant strain in the magnetic Ni layer. These pronounced changes and strain effects in the Ni layer result in a peak in coercivity.

When analyzing the reciprocal space map across the SPT, we observe a clear splitting of the V_2O_3 peak and a diagonal shift in the peak position along the Q_y direction, deviating from the anticipated symmetric pattern. This can be attributed to the presence of anti-phase boundaries, which introduce structural disorder and disrupt the regular lattice arrangement. As a result, deviations from the expected symmetry and stress distribution occur within the material. Our results reveal no periodic structural distortions in the reciprocal space map due to the simultaneous existence of two phases in the V_2O_3 layer. This could be attributed to the fact that the notable structural changes associated with the competing phases occur at a mesoscale, which exceeds the resolution capability of our measurement technique.

VI. SUPPLEMENTARY MATERIAL

See the supplementary material for structural measurements of the reference single-layer V_2O_3 sample. It also presents HAADF-STEM images of the V_2O_3/Ni film grown on the Al_2O_3 c-plane, along with detailed magnetic and structural data for the V_2O_3/Ni heterostructure deposited on the sapphire r-plane, and fitting information.

Acknowledgements
This work was supported by funding from the University of Iceland Research Fund, the Icelandic Research Fund Grant No. 207111. Instrumentation funding from the Icelandic Infrastructure Fund is acknowledged. This work is based on experiments performed at the BM28 (XMaS) beamline at the European Synchrotron Radiation Facility, Grenoble, France. XMaS is a National Research Facility funded by the UK EPSRC and managed by the Universities of Liverpool and Warwick. This project has received funding from the European Union's Horizon 2020 research and innovation program under grant agreement No 823717 – ESTEEM3.

Corresponding authors
U. B. Arnalds (uarnalds@hi.is)

Conflict of Interest There is no conflict of interest to disclose.

Data Availability Statement The data that support the findings of this study are available from the corresponding author upon reasonable request.

[1] C. Griffiths and H. Eastwood, Journal of Applied Physics **45**, 2201 (1974).
[2] D. Lee, B. Chung, Y. Shi, G.-Y. Kim, N. Campbell, F. Xue, K. Song, S.-Y. Choi, J. Podkaminer, T. Kim, *et al.*, Science **362**, 1037 (2018).
[3] M. Yang, Y. Yang, B. Hong, L. Wang, K. Hu, Y. Dong, H. Xu, H. Huang, J. Zhao, H. Chen, *et al.*, Scientific Reports **6**, 1 (2016).
[4] P. Homm, M. Menghini, J. Seo, S. Peters, and J.-P. Locquet, APL Materials **9**, 021116 (2021).
[5] S. Shin, S. Suga, M. Taniguchi, M. Fujisawa, H. Kanzaki, A. Fujimori, H. Daimon, Y. Ueda, K. Kosuge, and S. Kachi, Physical Review B **41**, 4993 (1990).
[6] M. Marezio, D. B. McWhan, J. Remeika, and P. Dernier, Physical Review B **5**, 2541 (1972).
[7] Z. Khan, P. Singh, S. A. Ansari, S. R. Manippady, A. Jaiswal, and M. Saxena, Small **17**, 2006651 (2021).
[8] J.-y. Kim, J. Cramer, K. Lee, D.-S. Han, D. Go, P. Salev, P. N. Lapa, N. M. Vargas, I. K. Schuller, Y. Mokrousov, *et al.*, Advanced Functional Materials **32**, 2111555 (2022).
[9] V. Baltz, A. Manchon, M. Tsoi, T. Moriyama, T. Ono, and Y. Tserkovnyak, Reviews of Modern Physics **90**, 015005 (2018).
[10] J. Guo, H. Zhou, J. Wang, W. Liu, M. Cheng, X. Peng, H. Qin, J. Wei, P. Jin, J. Li, *et al.*, Artificial Cells, Nanomedicine, and Biotechnology **46**, 58 (2018).
[11] Y. Wang, K.-M. Kang, M. Kim, H.-S. Lee, R. Waser, D. Wouters, R. Dittmann, J. J. Yang, and H.-H. Park, Materials today **28**, 63 (2019).
[12] Y. Zhou and S. Ramanathan, Proceedings of the IEEE **103**, 1289 (2015).
[13] M. Lee, *New Materials and Techniques for Resistive Switching Devices and Neuromorphic Computing*, Ph.D. thesis, UC San Diego (2021).
[14] J. Lappalainen, J. Mizsei, and M. Huotari, Journal of Applied Physics **125**, 044501 (2019).
[15] Y. Kalcheim, N. Butakov, N. M. Vargas, M.-H. Lee, J. Del Valle, J. Trastoy, P. Salev, J. Schuller, and I. K. Schuller, Physical Review Letters **122**, 057601 (2019).
[16] C. T. Wolowiec, J. G. Ramírez, M.-H. Lee, N. Ghazikhanian, N. M. Vargas, A. C. Basaran, P. Salev, and I. K. Schuller, Physical Review Materials **6**, 064408 (2022).
[17] D. A. Gilbert, J. G. Ramírez, T. Saerbeck, J. Trastoy, I. K. Schuller, K. Liu, and J. de la Venta, Scientific reports **7**, 1 (2017).
[18] J. De La Venta, S. Wang, J. Ramirez, and I. K. Schuller, Applied Physics Letters **102**, 122404 (2013).
[19] J. De La Venta, S. Wang, T. Saerbeck, J. Ramírez, I. Valmianski, and I. K. Schuller, Applied Physics Letters **104**, 062410 (2014).
[20] K. Ignatova, E. Thorsteinsson, B. Jósteinsson, N. Strandqvist, C. Vantaraki, V. Kapaklis, A. Devishvili, G. K. Pálsson, and U. Arnalds, Journal of Physics: Condensed Matter **34**, 495001 (2022).
[21] A. McLeod, E. Van Heumen, J. Ramirez, S. Wang, T. Saerbeck, S. Guenon, M. Goldflam, L. Anderegg, P. Kelly, A. Mueller, *et al.*, Nature Physics **13**, 80 (2017).
[22] V. Polewczyk, S. Chaluvadi, P. Orgiani, G. Panaccione, G. Vinai, G. Rossi, and P. Torelli, Physical Review Materials **5**, 034413 (2021).

[23] G. Wei, X. Lin, Z. Si, N. Lei, Y. Chen, S. Eimer, and W. Zhao, Applied Physics Letters **114**, 012407 (2019).

[24] U. B. Arnalds, J. S. Agustsson, A. S. Ingason, A. K. Eriksson, K. B. Gylfason, J. T. Gudmundsson, and S. Olafsson, Review of Scientific Instruments **78**, 103901 (2007).

[25] O. Bikondoa, L. Bouchenoire, S. D. Brown, P. B. J. Thompson, D. Wermeille, C. A. Lucas, M. J. Cooper, and T. P. A. Hase, Phil. Trans. R. Soc. A **377**, 20180237 (2019).

[26] M. Björck and G. Andersson, Journal of Applied Crystallography **40**, 1174 (2007).

[27] D. S. Su and R. Schlögl, Catalysis letters **83**, 115 (2002).

[28] J. Li, B. Gauntt, J. Kulik, and E. Dickey, Microscopy and Microanalysis **15**, 1004 (2009).

[29] G. Sun, X. Cao, X. Gao, S. Long, M. Liang, and P. Jin, Applied Physics Letters **109**, 143903 (2016).

[30] P. Hirsch, A. Howie, R. Nicholson, D. Pashley, and M. Whelan, London, UK **358** (1965), 10.1016/0022-3115(67)90194-8.

[31] B. W. David and C. B. Carter, *Transmission electron microscopy: A textbook for materials science* (Springer Science+ Business Media, LLC, 1996).

[32] X. Li, A. Gloter, H. Gu, X. Cao, P. Jin, and C. Colliex, Acta materialia **61**, 6443 (2013).

[33] J. Schoiswohl, M. Sock, S. Surnev, M. Ramsey, F. Netzer, G. Kresse, and J. N. Andersen, Surface Science **555**, 101 (2004).

[34] M. Luysberg, R. Sofin, S. Arora, and I. Shvets, Physical Review B **80**, 024111 (2009).

[35] C. Xu, H. Du, A. J. van der Torren, J. Aarts, C.-L. Jia, and R. Dittmann, Scientific reports **6**, 1 (2016).

[36] P. Dernier and M. Marezio, Physical Review B **2**, 3771 (1970).

[37] L. Eckert and R. Bradt, Journal of Applied Physics **44**, 3470 (1973).

[38] D. Rusu, J. J. Peters, T. P. Hase, J. A. Gott, G. A. Nisbet, J. Strempfer, D. Haskel, S. D. Seddon, R. Beanland, A. M. Sanchez, *et al.*, Nature **602**, 240 (2022).

[39] I. Valmianski, A. F. Rodríguez, J. Rodríguez-Álvarez, M. G. Del Muro, C. Wolowiec, F. Kronast, J. G. Ramírez, I. K. Schuller, A. Labarta, and X. Batlle, Nanoscale **13**, 4985 (2021).

[40] E. B. Thorsteinsson, S. Shayestehaminzadeh, and U. B. Arnalds, Applied Physics Letters **112**, 161902 (2018).